Frontal circulation and submesoscale variability during the formation of a Southern Ocean mesoscale eddy

Katherine A. Adams* and Philip Hosegood

School of Marine Science and Engineering, Plymouth University

John R. Taylor

Department of Applied Mathematics and Theoretical Physics, University of Cambridge

Jean-Baptiste Sallée

Sorbonne Universités, UPMC/CNRS, LOCEAN Laboratory

Scott Bachman

Department of Applied Mathematics and Theoretical Physics, University of Cambridge

Ricardo Torres

Plymouth Marine Laboratory

Megan Stamper

Department of Applied Mathematics and Theoretical Physics, University of Cambridge

**Corresponding author address:* School of Marine Science and Engineering, Plymouth University, Drake Circus, Plymouth, United Kingdom.

E-mail: kate.adams@plymouth.ac.uk

ABSTRACT

Observations made in the Scotia Sea during the May 2015 Surface Mixed Layer Evolution at Submesoscales (SMILES) research cruise captured submesoscale, O(1-10 km), variability along the periphery of a mesoscale O(10-100 km) meander precisely as it separated from the Antarctic Circumpolar Current (ACC) and formed a cyclonic eddy $\sim$ 120 km in diameter. The ACC meander developed in the Scotia Sea, an eddy-rich frontal region east of the Drake Passage where the Subantarctic and Polar fronts converge and modifications of Subantarctic mode water (SAMW) occur. A drifter triplet was followed with an undulating towed-CTD during a cross-front survey. *In situ* measurements reveal a rich submesoscale structure of temperature and salinity and a loss of frontal integrity along the newly-formed southern sector of the eddy. A mathematical framework to estimate vertical velocity is developed from co-located drifter and horizontal water velocity time series. Downwelling (upwelling) rates of O(100 m day^{-1}) are found in the northern (southern) eddy sector. Preconditioning for submesoscale instabilities is found in the mixed layer, particularly at the beginning of the survey in the vicinity of density fronts. Shallower mixed layer depths and increased stratification are observed later in the survey on the inner edge of the front. Evolution in T-S space indicates modification of water mass properties in the upper 200 m over 2 days. Modifications along σ_θ 27 - 27.2 kg m^{-3} have climate-related implications for mode and intermediate water transformation in the Scotia Sea on finer spatiotemporal scales than observed previously.

1. Introduction

The Southern Ocean hosts the most energetic current in the world, the Antarctic Circumpolar Current (ACC). Unbounded by land, the ACC connects ocean basins and transports an estimated 154 $\pm$ 38 Sv through the Drake Passage (Firing et al. 2011). The ACC is predominantly in geostrophic and thermal wind balance with sea surface height (SSH) gradients and lateral density gradients, or fronts. Large-scale instabilities in the balanced ACC flow cause mesoscale, O(10-100 km), meanders and eddies in the Southern Ocean. While the rich mesoscale structure of the ACC has been studied intensely, finer-scale variability along Southern Ocean fronts is less understood and observed.

Two of the most prominent fronts in the Southern Ocean are the Subantarctic and Polar fronts (hereafter, SAF and PF). Due to sparse data coverage in the Southern Ocean, altimetry-based frontal definitions have been developed; SSH_{SAF} = -0.25 m and SSH_{PF} = -0.70 m are updated values from Sallée et al. (2008). North of the SAF, water masses such as Subantarctic Mode water (SAMW) and Antarctic Intermediate water (AAIW), subduct along isopycnals at specific locations in the Southern Ocean, such as the Scotia Sea (Sallée et al. 2010). The subducted pools of SAMW and AAIW observed north of the ACC contain high levels of anthropogenic CO_2 (Sabine et al. 2004; Pardo et al. 2014) and heat (Frölicher et al. 2015). Currently, SAMW is thought to be transformed by air-sea buoyancy fluxes (Cerovecki et al. 2013) and subsequently mixed and subducted with AAIW, $\sigma_{\theta 27.2}$, to the South Atlantic (Sallée et al. 2010). In locations 'upstream' of the subducted SAMW/AAIW pools, mode water transformation occurs in the mixed layer at the SAF and has climatic implications. The large-scale, O(100-1000 km), physical processes responsible for the subduction of heat and carbon in SAMW/AAIW pools have been discussed and documented, e.g. Sallée et al. (2010, 2012), but very little is known about subduction associated with smaller scales processes (Naveira Garabato et al. 2001).

A potentially important class of dynamics responsible for modulating the vertical exchange at fronts in the Southern Ocean occurs at the submesoscale, O(1-10 km). The oceanic submesoscale is instrumental in extracting energy from density fronts in thermal wind balance and transferring the energy from mesoscale to submesoscale and dissipative scales (Thomas and Taylor 2010; Capet et al. 2008). The downscale transfer of energy results in ageostrophic motions with large vertical velocities, $O(100\text{ m day}^{-1})$ (Mahadevan and Tandon 2006; Capet et al. 2008; Thomas et al. 2008) capable of transporting heat and tracers across the base of the mixed layer. Where energetic submesoscale processes exist, the resulting vertical buoyancy fluxes may attain an importance equal to or greater than those forced by air-sea exchange.

The presence of fronts preconditions the mixed layer to the development of submesoscale processes, which are characterized by $O(1)$ Rossby (Ro) and balanced Richardson (Ri_B) numbers (Thomas et al. 2008). Submesoscale dynamics are often associated with hydrodynamic instabilities including mixed layer instability (MLI), symmetric instability (SI), and inertial instability (II) (Haine and Marshall 1998; Fox-Kemper et al. 2008; Thomas et al. 2008). These instabilities grow at the expense of available potential energy associated with lateral density gradients (MLI) or thermal wind kinetic energy (II and SI). In all cases, these instabilities are likely to develop at fronts and can significantly affect the mixed layer density structure (Boccaletti et al. 2007; Hosegood et al. 2008; Taylor and Ferrari 2009; Mahadevan et al. 2010).

Sampling submesoscale processes presents challenges due to the complex dynamics of the mixed layer and the short spatiotemporal scales of variability, from hours to days and meters to kilometers. Very few submesoscale-resolving measurements have been made in the Southern Ocean (Rocha et al. 2016), though a recent modeling study has demonstrated the dependence of submesoscale vertical velocities on an energetic mesoscale eddy and strain field (Rosso et al. 2015). An energetic submesoscale is, therefore, expected in a region with high mesoscale EKE, such as the Scotia Sea, a mesoscale eddy hot spot (Frenger et al. 2015). Large, high-*Ro* meanders of the SAF and PF fronts (Figure 2) are indicative of a highly energetic mesoscale field in the Scotia Sea region, suggesting the presence of a similarly energetic submesoscale field.

Here we present novel observations of submesoscale variability in the Southern Ocean from the SMILES (Surface Mixed Layer Evolution at Submesoscales) project, `http://www.smiles-project.org`. SMILES aims to (1) characterize submesoscale dynamics and (2) evaluate the role of submesoscales in mode water transformation in the Scotia Sea using a combination of observations and models. The observational component of the SMILES project consists of a single research cruise to the Scotia Sea in austral autumn 2015. During a drifter-following cross-front survey, a northward meander of the SAF and PF (Figure 2) separated from the ACC and formed a cold-core mesoscale eddy.

In this paper, we focus on the observed frontal circulation and submesoscale variability along the periphery of the newly-formed eddy. Data sources and processing methods are described in Section 2. Results from the drifter-following survey are presented as follows in Section 3: a) eddy formation, b) frontal circulation, c) cross-frontal variability, and d) water mass modification. Section 4 presents a submesoscale instability analysis and an estimation of vertical velocity. In Section 5, results are summarized and the implications of submesoscale processes during eddy formation in the Scotia Sea are discussed.

2. Data Sources and Methods

Ship-based data sources

The field component of the SMILES project consisted of a Scotia Sea research cruise, 22 April - 21 May 2015, performed aboard the British Antarctic Survey RRS James Clark Ross (JCR). Seasoar, a winged and towed CTD body equipped with a Seabird-Electronics Inc. SBE911, collected temperature, conductivity, and pressure measurements at 16 Hz. Seasoar data is collected in a saw-tooth pattern (Figure 3) at 8 knots ($\sim$ 4 m s^{-1}) with a horizontal spacing between apogees of 2 km for 200-m dives. Temperature and salinity variables were binned to 0.5 dbar intervals. Binned data were gridded using a 2-dimensional Gaussian interpolation scheme (Barnes 1964) with regular spacing, 0.5-km horizontal and 1-m vertical, and decorrelation radii of 1 km and 2 m (Figure 3c).

Horizontal water velocity data was collected in 8-m depth bins over 22 to 600 m of the water column by the ship-board RDI Ocean Sciences 75 kHz acoustic doppler current profiler (ADCP). The collected data was cleaned, corrected for ship speed and heading, and ensemble averaged to 150-second bins using Common Ocean Data Access System (CODAS) processing tools. North and east velocity components from 30 - 200 m were gridded to the same grid as the Seasoar data then rotated into along-front and cross-front velocity components using the drifter trajectories as explained below.

Drogued drifters

Semi-Lagrangian water velocity data was collected using a triplet of drogued drifters. The drifters consisted of a sealed buoy with GPS and satellite communications, a 'holey-sock' drogue 10-m long and 90-cm in diameter centered at 50-m depth, and 3.5 mm Dyneema line. This design provided a drag area ratio of 44 which is accurate to follow water parcels to within 1 cm s^{-1} (Sybrandy et al. 2009). Drifter location updates were received at 10-minute intervals.

The drifters were released along the northern portion of the meander, approximately three minutes apart. The release location was inside (south) of the maximum jet velocity and temperature gradient as shown in Figure 3a for the first Seasoar leg of the survey. The trajectory of the first drifter released, D16, was chosen to define the along-front direction, θ_{along} (Table 1) . The closest drifter crossing in time and space of each Seasoar leg is the reference for the center of the front, with cross-frontal distance increasing away from the meander and eddy center. Each leg was rotated to a cross-front heading, θ_{cross}, defined as the orthogonal direction to θ_{along} for each respective Seasoar leg (Table 1). Similarly, measured horizontal water velocities were rotated into along-front and cross-front components for each leg.

Remote data sources

Satellite sea surface temperature (SST) and sea surface height (SSH) data were used during the cruise and analysis for frontal and eddy detection. Both data sets are available daily on a 0.25° grid. Figure 2 is an example of the remote sensing data available during the SMILES cruise. The daily, gridded microwave SST data was downloaded from Remote Sensing Systems, (`http://www.remss.com`). SSH, or absolute dynamic topography, and altimetrically-derived geostrophic surface current data were downloaded from AVISO Cnes data center (`www.aviso.altimetry.fr`) (Pujol et al. 2016). Subantarctic front and Polar front positions are defined using SSH contours of -0.25 m and -0.7 m, respectively, updated from the mean frontal position definitions in Sallée et al. (2008).

3. Results

a. Eddy formation

A northward meander of the Subantarctic front (SAF) and Polar front (PF) developed along the Antarctic Circumpolar Current (ACC) (Figure 2) in late April 2015. This mesoscale, $O(100\text{ km})$, feature characterized by 4°C SST and 0.5-m SSH meridional changes in 50 km, formed just south of the North Scotia Ridge. Antarctic surface water, <2°C south of the PF (Orsi et al. 1995), is observed in the center of the meander. The vorticity Rossby number, $Ro = \zeta f^{-1}$, of the meander as calculated from altimetrically-derived geostrophic surface currents from 20 April is ~ 0.4, a very high value for the coarse altimetry data set compared to previous submesoscale-focused process studies, e.g. $Ro \sim 0.1$ in the North Pacific (Hosegood et al. 2013).

A triplet of drogued drifters released in the northwest sector of the meander on 08 May 2015 20:00 GMT was followed with the RRS JCR while towing the Seasoar CTD perpendicular to the drifter trajectories. The daily progression of SST, SSH, drifter trajectories and the ship track are presented in Figure 4 for 8-12 May 2015. At the time of the drifter release, 18 days after the SST and SSH observations presented in Figure 2, the meander had sharpened yet remained tethered to the ACC as observed by SST and SSH fields, Figure 4a. During the survey, the drifters initially traveled east (Figure 4b) and southeast (Figure 4c) around the meander and remarkably continued along a cyclonic trajectory precisely as the meander separated from the ACC and formed a cold closed-core eddy, Figure 4c-e. Initially the cyclonic eddy measured approximately 120-km in diameter with a dynamic height anomaly of 0.5 m (-0.2 to -0.7 m SSH). After the eddy formed, Figure 4e, the SAF and PF returned to a zonal orientation south of the eddy. Hereafter, the meander/eddy feature will be referred to as an eddy for the duration of the Seasoar survey.

The Seasoar survey, shown as the ship track in Figure 4, consisted of 25 sections around the edge of the eddy ranging from 25 - 40 km in length. Maps of 10-m depth temperature and salinity from these 25 sections are presented in Figure 5a-b. The beginning northern sector of the survey is characterized by sharp temperature and salinity fronts (2°C, 0.2 psu in 2 km at 4-m depth) with warm, salty water outside and cold, fresh waters inside the eddy. A region characterized by a loss of temperature and salinity frontal integrity is observed along the southern portion of the survey. Submesoscale streamers or filaments only a few kilometers across are observed in the newly-formed southern sector of the eddy.

Horizontal water velocities measured at 50-m depth are included in Figure 5c-d where the along-front and cross-front components are determined relative to a drifter trajectory direction (Table 1) for each Seasoar section. A $\sim$ 70% decrease (1.5 to 0.4 m s^{-1}) in drifter and along-front water velocities is observed from the N to S legs. A sign change in cross-frontal velocities on either side of the drifters indicates confluent flow during the majority of the survey with diffluent cross-frontal flow in the southern portion of the survey.

Wind forcing during the Seasoar survey was unusually calm for April in the Southern Ocean with wind speeds < 10 m s^{-1} and winds from SE to NW rather than the expected westerlies.

Infared SST data are a resource for submesoscale studies due to the high, O(1 km), horizontal resolution. Due to heavy cloud cover very few infared SST images are available during the SMILES cruise. Partial coverage of the eddy during the Seasoar survey was captured by the an AVHRR sensor aboard the Metop-a satellite on 11 May 2015 at 12:42 GMT (Figure 6a). Unfortunately the southern and western sectors of the eddy were masked by clouds. The ship's underway temperature data at 4-m depth is overlaid on the infared SST data in Figure 6b. The comparison suggests a northward movement of the eddy since the beginning of the survey 2.5 days earlier. For comparison, the ship's temperature data is also plotted atop optimally-interpolated microwave

SST data for 11 May 2015. The eddy boundary, defined by the 3°C isotherm in Figure 6a and c is drastically different between the 1-km infared and coarser microwave SST data.

b. Cross-frontal variability

Vertical cross-sections of potential density anomaly (σ_θ, kg m^{-3}), temperature (°C), salinity, and horizontal water velocities (m s^{-1}) are presented in Figure 7 for the Seasoar legs labeled in Figure 5. The five sections span approximately two days and 180 degrees of heading of the drifter-following survey. Each section is referenced in a similar manner with respect to the front; the left (right) -hand side of the sections will be referred to as inner (outer) with negative (positive) cross-frontal distance. Since the sections are centered using the drifter trajectories, a cross-frontal distance of zero is not an explicit definition of the frontal center with respect to density.

In Leg N, σ_θ increases laterally away from the eddy core except for a dense filament $\sim$ 5 km in width located in the center of the leg (Figure 7a). The dense filament is observed between the 27.0 kg m^{-3} isopycnal (hereafter $\sigma_{\theta 27}$) which outcrops on either side of the filament. The inner lateral density gradient, 0.09 kg m^{-3} in 5 km, is nearly twice the gradient on the warm, outer side of the dense filament, 0.04 kg m^{-3} in 5 km. The $\sigma_{\theta 27}$ is observed subsurface in Leg E. The depth of the $\sigma_{\theta 27}$ is much shallower on the inner side of Leg S.

Mixed layer depth, MLD, defined as the level of a 0.01 kg m^{-3} density increase from the surface-most measurement, is included in Figure 7a. Values of MLD are O(100 m) for most of Leg N. In each leg, the mixed layer is shallowest within the density fronts, <50 m, and deepest within the dense filament at 130 m. The MLD shoals similarly to $\sigma_{\theta 27}$ in Leg S, suggestive of restratification of the inner front along the newly-formed sector of the eddy. The shallower MLD may be the result of temporal variability, e.g., restratification from submesoscale instabilities, or spatial variability.

Temperature and salinity fields vary similarly across the sections, Figure 7b-c, due to strong density compensation, characteristic of ACC fronts. In Leg N, the warm, salty outer region lies adjacent to a cold, dense filament at a cross-front distance of 0 km. Leg E, in the east sector of the survey, contains a small subsurface cold water intrusion at 120-m depth and 10-km cross-front distance. Intrusions of cold, fresh water on the outer side and warm, salty water on the inner side are observed in all legs collected in the east and southeast sectors of the survey. In leg SE, the intrusion is larger in vertical and horizontal extent and outcropped. In Leg S a loss of frontal integrity is observed compared to the well-organized, separated cold-fresh inner and warm-salty outer regions present at the start of the survey.

Vertical cross-sections of along-front and cross-front velocities, Figure 7d-e, show a strong barotropic component to the flow. Trends throughout the survey agree with the 50-m maps in Figure 5c-d. Along-front velocities decrease whereas cross-front velocities switch from confluent to diffluent from Legs N to S.

c. Frontal circulation

The frontal circulation at the center of each Seasoar leg can be described using the co-located drifter and horizontal water velocity datasets. As shown in Figure 8a, the drifter and along-front water velocities at 50-m depth are in strong agreement. Drifters initially deployed in the northern sector of the cyclonic eddy decelerated around the eastern side toward the southern sector where the along-front velocity is minimum, after which the drifters accelerated around the western edge. Similar trends were observed in the measured along-front velocity. The cross-frontal gradient of cross-frontal velocity, was negative (confluent) during the along-front deceleration and positive (diffluent) during the along-front acceleration as shown in (Figure 8b). In a horizontally non-divergent flow regime, cross-frontal confluence leads to along-front divergence and vice versa.

However, the deceleration of the drifters suggests convergent along-front flow in a region with convergent along-front flow and therefore the presence of a vertical circulation. These observations suggest downwelling occurred along the N - SE sectors and upwelling in the S survey sector. This will be quantified in Section 4b.

d. Water mass modification

The sharp temperature and salinity fronts across the eddy boundary indicate the presence of different water masses. T-S histograms for Seasoar sections N-S, Figure 9, show the prevalence of measurements in 0.15°C and 0.015 salinity bins. In Leg N the T-S measurements largely populate two separate regions in T-S space, with cold, fresh inner waters in the bottom left of the diagram and the warm, salty (spicy) outer region measurements in the top right. The two regions in T-S space are connected via $\sigma_{\theta\,27}$, the isopycnal that outcrops on either side of the dense filament at the front center in Leg N, previously presented in Figure 7. A similar connection along deeper isopycnals, such as $\sigma_{\theta\,27.2}$, is not observed in Leg N (Figure 9). This is due to an unequal isopycnal upheaval across the Seasoar leg and the 200-m depth limit of the dataset.

A cross-front exchange is observed in Legs NE-E as cool, fresh measurements $\sigma_{\theta\,27\,\text{-}\,27.2}$ extend into warmer and saltier T-S space. Along isopycnal exchange of T-S properties is less clear in Leg SE. By Leg S, the T-S space is fully populated indicating mixing or advection of new water masses, not previously observed at the start of the survey. The exchange or modification along $\sigma_{\theta\,27.1\,\text{-}\,27.2}$ suggests that water mass properties below the MLD are affected on timescales of O(1 day) and horizontal length scales of O(1-10 km) during the formation of this mesoscale eddy.

4. Analysis

a. Submesoscale instabilities

Although direct measurements of submesoscale instabilities were not made during the Seasoar survey, it is possible to diagnose whether conditions were favorable, or preconditioned, for submesoscale instability growth and which specific instabilities were possible (Thomas et al. 2013; Thompson et al. 2016). First, instability development is favored when Ertel potential vorticity (EPV),

$$EPV = \omega_{\mathbf{a}} \cdot \nabla b = (\boldsymbol{f} + \nabla \times \mathbf{u}) \cdot \nabla b, \tag{1}$$

is the opposite sign of f (Haine and Marshall 1998; Thomas et al. 2008); the absolute vorticity, ω_a, is the sum of planetary and relative vorticity and buoyancy is $b = -g\rho'\rho_0^{-1}$. The perturbation density, ρ', is the measured density, ρ, minus the average leg density, ρ_0. Expanding (1) gives

$$EPV = (w_y - v_z)b_x + (u_z - w_x)b_y + [f + (v_x - u_y)]b_z, \tag{2}$$

where subscripts indicate a partial derivative and x and y are the along-front and cross-front directions. Neglecting ∂x terms in (2) assumes along-front gradients $\ll$ cross-front gradients. This simplification yields,

$$EPV \simeq (f - u_y)b_z + u_z b_y, \tag{3}$$

an approximation for EPV dependent on cross-front and vertical gradients in the along-front velocity and buoyancy. The 2-dimensional approximations of EPV (3) is shown in Figure 10 along with the cross-frontal buoyancy gradient at 10-m depth to identify the density fronts in each leg.

EPV, defined in (3) for Legs N-S is shown in Figure 10b. Regions with EPV $>$ 0 are preconditioned for the instabilities described above and are observed on either side of the lateral buoyancy gradients, or fronts, and mostly above the MLD. The band of negative EPV in each leg is stable to instabilities due to the strong vertical stratification, b_z, of the ML base.

For regions where EPV > 0, since $f < 0$, specific submesoscale instabilities can be identified using the balanced Richardson number, $Ri_B = f^2 b_z^2 b_y^{-4}$. The criteria presented in Thomas et al. (2013) classifies gravitational ($Ri_B < -1$), mixed gravitational-symmetric ($-1 < Ri_B < 0$), symmetric ($0 < Ri_B < 1$), and inertial ($1 < Ri_B < Ro^{-1}$) instabilities, as well as stable portions of the water column, $Ri_B > Ro^{-1}$.

Locations favored for specific submesoscale instabilities as diagnosed by Ri_B are presented in Figure 10c. Throughout the survey, the mixed layer was consistently more susceptible to submesoscale instabilities than the deep, stable regions where EPV<0. Gravitational instability is most likely early in the survey and away from density fronts where MLD are large. The criteria for mixed and symmetric instabilities are met within density fronts in Legs N - E. Conditions conducive for inertial, or centrifugal, instability are not common in this survey however the few instances are located on the outer (right-hand) side with $Ro = \zeta f^{-1} < 0$, an anticyclonic sense.

Regions where conditions are conducive to the development of submesoscale instabilities are shown as a fraction of the mixed layer in Figure 10d. There is a general decrease between the N and S legs, indicating a greater proportion of the ML is more prone to instabilities earlier in the survey versus in the legs collected in the southern sector of the eddy. Throughout the survey, the majority of the instability indications are for gravitational with conditions favorable for symmetric or mixed gravitational and symmetric concentrated near lateral density gradients.

b. Estimation of vertical velocity

Vertical velocities, w, were not directly measured in the SMILES Seasoar survey. However, the co-located drifter and ADCP datasets allow for the following mathematical framework which yields a solvable expression for w at a specific depth and a cross-frontal location in each Seasoar leg.

Let $\mathbf{x}_D(t)$, and $\mathbf{u}_D(t)$ be the measured drifter position and velocity vectors at time t where

$$\left(\frac{dx_D}{dt}, \frac{dy_D}{dt}\right) = \left(u_D(t), v_D(t)\right). \tag{4}$$

Let $\mathbf{u}_E(x,y,z,t)$ be the Eulerian fluid velocity. Assume that the drifter moves with the vertically averaged Eulerian velocity at the horizontal location of the drogue from depth z_1 to z_2

$$\frac{d\mathbf{u}_D}{dt} = \frac{d}{dt}\left[\bar{\mathbf{u}}_E(x_D(t), y_D(t), t)\right] \tag{5}$$

where

$$\bar{\mathbf{u}}_E \equiv \frac{1}{z_1 - z_2}\int_{z_2}^{z_1} \mathbf{u}_E \, dz. \tag{6}$$

Here we set $z_1 = 0$ at the surface and $z_2 = 50$ m, the drifter drogue depth. This assumes the drogued drifter is moving with the depth-averaged Eulerian velocity in the top 50-m of the water column, Figure 8a. Expanding the derivative in (5),

$$\frac{d\mathbf{u}_D}{dt} = \frac{\partial \bar{\mathbf{u}}_E}{\partial t} + \frac{dx_D}{dt}\frac{\partial \bar{\mathbf{u}}_E}{\partial x} + \frac{dy_D}{dt}\frac{\partial \bar{\mathbf{u}}_E}{\partial y} = \frac{\partial \bar{\mathbf{u}}_E}{\partial t} + \bar{\mathbf{u}}_E \cdot \nabla_H \bar{\mathbf{u}}_E. \tag{7}$$

where $\nabla_H \equiv (\frac{\partial}{\partial x}, \frac{\partial}{\partial y})$. From continuity, $\nabla \cdot \mathbf{u}_E \equiv 0$ hence $\nabla \cdot \bar{\mathbf{u}}_E = 0$ for constant z_1 and z_2,

$$\frac{\partial \bar{u}_E}{\partial x} + \frac{\partial \bar{v}_E}{\partial y} + \frac{w_E(x_D, y_D, z_1, t) - w_E(x_D, y_D, z_2, t)}{z_1 - z_2} = 0. \tag{8}$$

From (7), the rate of change of the along-front drifter velocity is

$$\frac{du_D}{dt} = \frac{\partial \bar{u}_E}{\partial t} + \bar{u}_E \frac{\partial \bar{u}_E}{\partial x} + \bar{v}_E \frac{\partial \bar{u}_E}{\partial y} \tag{9}$$

while (8) gives

$$\frac{\partial \bar{u}_E}{\partial x} = -\frac{\partial \bar{v}_E}{\partial y} - \frac{w_E|_{z_1} - w_E|_{z_2}}{z_1 - z_2}. \tag{10}$$

Substituting (10) in (9) gives

$$\frac{du_D}{dt} = \frac{\partial \bar{u}_E}{\partial t} - \bar{u}_E \frac{\partial \bar{v}_E}{\partial y} - \bar{u}_E \frac{w_E|_{z_1} - w_E|_{z_2}}{z_1 - z_2} + \bar{v}_E \frac{\partial \bar{u}_E}{\partial y}. \tag{11}$$

Re-arranging (11) yields an expression for the difference of vertical velocity from z_1 to z_2

$$w_E\big|_{z_1} - w_E\big|_{z_2} = (z_1 - z_2)\left[-\frac{1}{\bar{u}_E}\frac{du_D}{dt} + \frac{1}{\bar{u}_E}\frac{\partial \bar{u}_E}{\partial t} - \frac{\partial \bar{v}_E}{\partial y} + \frac{\bar{v}_E}{\bar{u}_E}\frac{\partial \bar{u}_E}{\partial y}\right]. \tag{12}$$

An expression for w_E at the drogue depth, z_2, is obtained by setting $w_E(z_1 = 0) = 0$,

$$w_E\big|_{z_2} = z_2\left[\frac{1}{\bar{u}_E}\frac{du_D}{dt} - \frac{1}{\bar{u}_E}\frac{\partial \bar{u}_E}{\partial t} + \frac{\partial \bar{v}_E}{\partial y} - \frac{\bar{v}_E}{\bar{u}_E}\frac{\partial \bar{u}_E}{\partial y}\right]. \tag{13}$$

If we assume

$$\frac{\partial \bar{u}_E}{\partial t} \ll \frac{du_D}{dt} \tag{14}$$

and

$$\left|\frac{\bar{v}_E}{\bar{u}_E}\frac{\partial \bar{u}_E}{\partial y}\right| \ll \left|\frac{\partial \bar{v}_E}{\partial y}\right| \tag{15}$$

then

$$w_E\big|_{z_2} \simeq z_2\left[\frac{1}{\bar{u}_E}\frac{du_D}{dt} + \frac{\partial \bar{v}_E}{\partial y}\right]. \tag{16}$$

Expression (16) allows for the calculation of vertical velocity at depth z_2. For the SMILES Seasoar survey, w is estimated in the center of each Seasoar leg at the drifter drogue depth of 50 m (Figure 8d). Velocity components $\bar{u}_E$ and $\bar{v}_E$ are calculated by averaging velocities from the first good ADCP bin, 30-m, to 50-m, as in Figure 8a. The cross-frontal velocity gradients, $\frac{\partial \bar{u}_E}{\partial y}$ and $\frac{\partial \bar{v}_E}{\partial y}$, are averaged +/- 1-km from the center of each Seasoar leg (Figure 8b).

Vertical velocities calculated from (16) are presented in Figure 8d with negative (positive) values during the N-SE (S) eddy survey sectors. As deduced qualitatively in Section 3b, the pairing of drifter deceleration and confluence yields downwelling, or subduction while upwelling is expected during drifter acceleration and diffluent flow. The estimated magnitudes of $w_E|_{50m}$, O(100 m day^{-1}), are similar to reported values for submesoscale processes, however, we can not discern the relative contributions of the mesoscale and submesoscale vertical motions here.

The scaling simplification made in (15) is verified in Figure 8c. The steady state assumption in (14) is checked using altimetry and drifter data sets. The average Eulerian acceleration, $\frac{\partial \bar{u}_E}{\partial t}$, estimated from altimetrically-derived geostrophic surface currents (not shown), are 0.04 ± 0.02 m s^{-1} per day which is an order of magnitude smaller than the average measured drifter accelerations, 0.49 ± 0.29 m s^{-1} per day) and the opposite sign as an expected change in along-front velocity due to the cyclonic eddy rotation.

5. Discussion & Summary

Here we have presented high-resolution observations across the ACC as a cyclonic eddy formed in the Scotia Sea. The novel observations reveal submesoscale frontal variability and two distinct dynamic regimes along the periphery of the eddy, depicted in Figure 11. In the northern to eastern regime of the survey, confluence and deceleration were observed in the cross-front and along-front directions, respectively. Along the newly-formed southern edge of the eddy, along-front acceleration and cross-front diffluent flow is observed coincident with a complex T-S structure, similar to submesoscale features found in other studies, e.g. filaments and streamers (Gula et al. 2014; Klymak et al. 2016). A submesoscale instability analysis identified regions across each cross-frontal section prone to the development of gravitational, mixed, symmetric and inertial instabilities. Preconditioning for mixed and symmetric instabilities was found near large cross-frontal density gradients in the mixed layer throughout the survey. Despite the loss of frontal integrity observed in the southern regime, the eddy discussed here maintained a distinct signature in SST and SSH over the following two months as evidenced by remote sensing imagery.

A mathematical framework for estimating vertical velocity, derived in Section 4b, yields w = $O(100 \text{ m day}^{-1})$ with upwelling in the first regime and downwelling in the second, southern regime (Figure 11). Although there is a lack of *in situ* vertical velocity observations available for comparison, w of $O(100 \text{ m day}^{-1})$ have been consistently reported in submesoscale-resolving numerical models compared to mesoscale estimates of $O(10 \text{ m day}^{-1})$ (Lévy et al. 2001; Capet et al. 2008; Rosso et al. 2014). The relative contributions from submesoscale and mesoscale mechanisms cannot be quantified with the extant dataset; however, submesoscale dynamics along the periphery of the eddy might contribute to the large vertical velocities reported here.

The Scotia Sea hosts an especially high abundance of mesoscale eddies (Frenger et al. 2015) in the eddy-rich Southern Ocean. Eddy kinetic energy (EKE) in this region, calculated from time-mean removed, altimetry-derived geostrophic surface currents (AVISO; 1993-2015) is O(0.1 - 1 m^2 s^{-2}). Recent submesoscale-resolving modeling results indicate a strong correlation between mesoscale EKE and submesoscale vertical velocity in the Southern Ocean (Rosso et al. 2015) implicating a downscale energy transfer. Although the Scotia Sea EKE values and w esimates presented here are much higher than the domain-averaged magnitudes reported inRosso et al. (2015), the trend of high EKE and high w is consistent.

The strong vertical circulation found at the SAF, suggests that submesoscale processes might be critical in transforming and subducting mode and intermediate waters, although such processes have been mostly ignored in previous studies. Water mass properties across the frontal region were initially observed as a cold, fresh eddy region and a warm, salty outer region. The rapid spread in T-S space suggests mixing occurred during the eddy formation. Enhanced vertical circulation and mixing, prompted by submesoscale processes, have the potential to transform mode and intermediate water density classes and contribute to the uptake of anthropogenic heat and carbon to the Southern Ocean. A quantification of the net water-mass subduction associated with the observed circulation will be part of a future study.

Cyclonic mesoscale eddies have been observed with high chlorophyll signatures in the Scotia Sea (Kahru et al. 2007), implicating their importance on primary production in the region. Studies resolving submesoscale dynamics in mesoscale eddies have shown that strong vertical velocities, like those presented here, may drive the vertical exchange in the upper ocean with important effects on nutrient supply to the photic zone (Lévy et al. 2001; Mahadevan et al. 2008; Lévy et al. 2012; Mahadevan 2016). The biogeochemical responses within the eddy observed during the SMILES cruise are a focus of a future study.

Acknowledgments. The SMILES project is funded through the National Environmental Research Council, standard grant NE/J009857/1. JR311 data collection and technical support were received from the British Antarctic Survey, the crew of RRS James Clark Ross, and the NEODAAS and PML remote sensing groups. Seasoar operations were led by National Marine Facilities technicians Paul Provost, Dougal Mountifield, Julie Wood, and Candice Cameron, from the UK National Oceanographic Centre. Peter Ganderton designed and built the drifter electronics package. The altimeter products were produced by Ssalto/Duacs and distributed by Aviso, with support from Cnes (http://www.aviso.altimetry.fr/duacs/). Microwave OI SST data are produced by Remote Sensing Systems and sponsored by National Oceanographic Partnership Program (NOPP) and the NASA Earth Science Physical Oceanography Program.

References

Barnes, S. L., 1964: A Technique for Maximizing Details in Numerical Weather Map Analysis. Journal of Applied Meteorology, 396–409 pp.

Boccaletti, G., R. Ferrari, and B. Fox-Kemper, 2007: Mixed layer instabilities and restratification. *Journal of Physical Oceanography*, **37**, 2228–2250, doi:10.1175/JPO3101.1.

Capet, X., J. C. McWilliams, M. J. Molemaker, and A. F. Shchepetkin, 2008: Mesoscale to Submesoscale Transition in the California Current System. Part I: Flow Structure, Eddy Flux, and Observational Tests. *Journal of Physical Oceanography*, **38 (1)**, 29–43, doi:10.1175/2007JPO3671.1, URL http://journals.ametsoc.org/doi/abs/10.1175/2007JPO3671.1.

Cerovecki, I., L. D. Talley, M. R. Mazloff, and G. Maze, 2013: Subantarctic Mode Water Formation, Destruction, and Export in the Eddy-Permitting Southern Ocean State Estimate. *Journal of Physical Oceanography*, **43 (7)**, 1485–1511, doi:10.1175/JPO-D-12-0121.1, URL http://journals.ametsoc.org/doi/abs/10.1175/JPO-D-12-0121.1.

Firing, Y. L., T. K. Chereskin, and M. R. Mazloff, 2011: Vertical structure and transport of the Antarctic Circumpolar Current in Drake Passage from direct velocity observations. *Journal of Geophysical Research*, **116 (C8)**, C08 015, doi:10.1029/2011JC006999, URL http://doi.wiley.com/10.1029/2011JC006999.

Fox-Kemper, B., R. Ferrari, and R. Hallberg, 2008: Parameterization of Mixed Layer Eddies. Part I: Theory and Diagnosis. *J Phys Oceanogr*, **38 (6)**, 1145–1165, URL http://journals.ametsoc.org/doi/abs/10.1175/2007JPO3792.1.

Frenger, I., M. Münnich, N. Gruber, and R. Knutti, 2015: Southern Ocean eddy phenomenology. *Journal of Geophysical Research: Oceans*, **120 (11)**, 7413–7449, doi:10.1002/2015JC011047, URL http://doi.wiley.com/10.1002/2015JC011047.

Frölicher, T. L., and Coauthors, 2015: Dominance of the Southern Ocean in Anthropogenic Carbon and Heat Uptake in CMIP5 Models. *Journal of Climate*, **28 (2)**, 862–886, doi:10.1175/JCLI-D-14-00117.1.

Gula, J., M. J. Molemaker, and J. C. McWilliams, 2014: Submesoscale cold filaments in the Gulf Stream. *Journal of Physical Oceanography*, **44 (10)**, 140728145042 006, doi:10.1175/JPO-D-14-0029.1, URL http://journals.ametsoc.org/doi/abs/10.1175/JPO-D-14-0029.1.

Haine, T. W. N., and J. Marshall, 1998: Gravitational, Symmetric, and Baroclinic Instability of the Ocean Mixed Layer. *Journal of Physical Oceanography*, **28 (4)**, 634–658, doi:10.1175/

1520-0485.

Hosegood, P. J., M. C. Gregg, and M. H. Alford, 2008: Restratification of the Surface Mixed Layer with Submesoscale Lateral Density Gradients: Diagnosing the Importance of the Horizontal Dimension. *Journal of Physical Oceanography*, **38 (11)**, 2438–2460, doi:10.1175/2008JPO3843.1, URL http://journals.ametsoc.org/doi/abs/10.1175/2008JPO3843.1.

Hosegood, P. J., M. C. Gregg, and M. H. Alford, 2013: Wind-driven submesoscale subduction at the north Pacific subtropical front. *Journal of Geophysical Research: Oceans*, **118 (10)**, 5333–5352, doi:10.1002/jgrc.20385, URL http://doi.wiley.com/10.1002/jgrc.20385.

Kahru, M., B. G. Mitchell, S. T. Gille, C. D. Hewes, and O. Holm-Hansen, 2007: Eddies enhance biological production in the Weddell-Scotia Confluence of the Southern Ocean. *Geophysical Research Letters*, **34 (14)**, L14 603, doi:10.1029/2007GL030430, URL http://doi.wiley.com/10.1029/2007GL030430.

Klymak, J. M., and Coauthors, 2016: Submesoscale streamers exchange water on the north wall of the Gulf Stream. *Geophysical Research Letters*, **43 (3)**, 1226–1233, doi:10.1002/2015GL067152, URL http://doi.wiley.com/10.1002/2015GL067152.

Lévy, M., R. Ferrari, P. J. S. Franks, A. P. Martin, and P. Rivière, 2012: Bringing physics to life at the submesoscale. *Geophysical Research Letters*, **39 (14)**, n/a–n/a, doi:10.1029/2012GL052756, URL http://doi.wiley.com/10.1029/2012GL052756.

Lévy, M., P. Klein, and A.-M. Treguier, 2001: Impact of sub-mesoscale physics on production and subduction of phytoplankton in an oligotrophic regime. *Journal of Marine Research*, **59 (4)**, 535–565, doi:10.1357/002224001762842181.

Mahadevan, A., 2016: The Impact of Submesoscale Physics on Primary Productivity of Plankton. *Annual review of marine science*, **8**, 161–84, doi:10.1146/annurev-marine-010814-015912, URL http://www.ncbi.nlm.nih.gov/pubmed/26394203.

Mahadevan, A., and A. Tandon, 2006: An analysis of mechanisms for submesoscale vertical motion at ocean fronts. *Ocean Modelling*, **14 (3-4)**, 241–256, doi:10.1016/j.ocemod.2006.05.006, URL http://www.sciencedirect.com/science/article/pii/S1463500306000540.

Mahadevan, A., A. Tandon, and R. Ferrari, 2010: Rapid changes in mixed layer stratification driven by submesoscale instabilities and winds. *Journal of Geophysical Research*, **115 (C3)**, C03 017, doi:10.1029/2008JC005203, URL http://doi.wiley.com/10.1029/2008JC005203.

Mahadevan, A., L. N. Thomas, and A. Tandon, 2008: Comment on ”Eddy/Wind Interactions Stimulate Extraordinary Mid-Ocean Plankton Blooms”. *Science*, **320 (448b)**, doi:10.1126/science.1152111.

Naveira Garabato, A. C., and Coauthors, 2001: Mesoscale Subduction at the Antarctic Polar Front Driven by Baroclinic Instability. *Journal of Physical Oceanography*, **31 (8)**, 2087–2107, doi:10.1175/1520-0485, URL http://journals.ametsoc.org/doi/abs/10.1175/1520-0485.

Orsi, A. H., T. Whitworth III, and W. D. Nowlin, 1995: On the meridional extent and fronts of the Antarctic Circumpolar Current. *Deep-Sea Research I*, **42 (5)**, 641–673.

Pardo, P. C., F. Pérez, S. Khatiwala, and A. Ríos, 2014: Anthropogenic CO2 estimates in the Southern Ocean: Storage partitioning in the different water masses. *Progress in Oceanography*, **120**, 230–242, doi:10.1016/j.pocean.2013.09.005.

Pujol, M.-I., Y. Faugère, G. Taburet, S. Dupuy, C. Pelloquin, M. Ablain, and N. Picot, 2016: DUACS DT2014 : the new multi-mission altimeter dataset reprocessed over 20 years. *Ocean*

Science Discussions, **0**, 1–48, doi:10.5194/os-2015-110, URL http://www.ocean-sci-discuss.net/os-2015-110/.

Rocha, C. B., T. K. Chereskin, S. T. Gille, and D. Menemenlis, 2016: Mesoscale to Submesoscale Wavenumber Spectra in Drake Passage. *Journal of Physical Oceanography*, **46 (2)**, 601–620, doi:10.1175/JPO-D-15-0087.1, URL http://journals.ametsoc.org/doi/10.1175/JPO-D-15-0087.1.

Rosso, I., A. M. Hogg, A. E. Kiss, and B. Gayen, 2015: Topographic influence on submesoscale dynamics in the Southern Ocean. *Geophysical Research Letters*, **42 (4)**, 1139–1147, doi:10.1002/2014GL062720, URL http://doi.wiley.com/10.1002/2014GL062720.

Rosso, I., A. M. Hogg, P. G. Strutton, A. E. Kiss, R. Matear, A. Klocker, and E. van Sebille, 2014: Vertical transport in the ocean due to sub-mesoscale structures: Impacts in the Kerguelen region. *Ocean Modelling*, **80**, 10–23, doi:10.1016/j.ocemod.2014.05.001, URL http://www.sciencedirect.com/science/article/pii/S146350031400064X.

Sabine, C. L., and Coauthors, 2004: The oceanic sink for anthropogenic CO2. *Science (New York, N.Y.)*, **305 (5682)**, 367–71, URL http://science.sciencemag.org/content/305/5682/367.abstract.

Sallée, J.-B., R. J. Matear, S. R. Rintoul, and A. Lenton, 2012: Localized subduction of anthropogenic carbon dioxide in the Southern Hemisphere oceans. *Nature Geoscience*, **5 (8)**, 579–584, doi:10.1038/ngeo1523, URL http://www.nature.com/doifinder/10.1038/ngeo1523.

Sallée, J. B., K. Speer, and R. Morrow, 2008: Response of the Antarctic Circumpolar Current to Atmospheric Variability. *Journal of Climate*, **21 (12)**, 3020–3039, doi:10.1175/2007JCLI1702.1, URL http://journals.ametsoc.org/doi/abs/10.1175/2007JCLI1702.1.

Sallée, J.-B., K. Speer, S. Rintoul, and S. Wijffels, 2010: Southern Ocean Thermocline Ventilation. *Journal of Physical Oceanography*, **40 (3)**, 509–529, doi:10.1175/2009JPO4291.1, URL http://journals.ametsoc.org/doi/abs/10.1175/2009JPO4291.1.

Sybrandy, A. L., P. P. Niiler, C. Martin, W. Scuba, E. Charpentier, and D. T. Meldrum, 2009: Global Drifter Programme: Barometer Drifter Design Reference, DBCP Report No.4, Rev 2.2. Tech. rep.

Taylor, J. R., and R. Ferrari, 2009: On the equilibration of a symmetrically unstable front via a secondary shear instability. *Journal of Fluid Mechanics*, **622**, 103, doi:10.1017/S0022112008005272.

Thomas, L. N., A. Tandon, and A. Mahadevan, 2008: Submesoscale processes and dynamics. *Ocean Modeling in an Eddying Regime*, H. Hecht, M., Hasume, Ed., American Geophysical Union, Washington, D. C., 17–38, doi:10.1029/177GM04, URL http://doi.wiley.com/10.1029/177GM04.

Thomas, L. N., and J. R. Taylor, 2010: Reduction of the usable wind-work on the general circulation by forced symmetric instability. *Geophysical Research Letters*, **37 (18)**, doi:10.1029/2010GL044680, URL http://doi.wiley.com/10.1029/2010GL044680.

Thomas, L. N., J. R. Taylor, R. Ferrari, and T. M. Joyce, 2013: Symmetric instability in the Gulf Stream. *Deep Sea Research Part II: Topical Studies in Oceanography*, **91**, 96–110, doi:10.1016/j.dsr2.2013.02.025, URL http://www.sciencedirect.com/science/article/pii/S0967064513000829.

Thompson, A. F., A. Lazar, C. Buckingham, A. C. Naveira Garabato, G. M. Damerell, and K. J. Heywood, 2016: Open-Ocean Submesoscale Motions: A Full Seasonal Cycle of Mixed Layer

Instabilities from Gliders. *Journal of Physical Oceanography*, **46 (4)**, 1285–1307, doi:10.1175/JPO-D-15-0170.1, URL http://journals.ametsoc.org/doi/10.1175/JPO-D-15-0170.1.

LIST OF TABLES

TABLE 1. True drifter and Seasoar leg headings. The along-front direction, θ_{along}, is defined by the drifter, D16, trajectory. The cross-front direction, θ_{cross}, is θ_{along} - 90. The mean true heading of Seasoar legs, θ_{leg}, are calculated with cross-front distance increasing away from the eddy center. Legs are projected onto a cross-frontal axis through a rotation of $\theta_{rot} = \theta_{cross} - \theta_{leg}$. The axis projection alters the horizontal spacing of survey measurements by the multiplication factor, $\cos(\theta_{rot})$. Legs labeled N-S correspond to section labels in Figure 5.

Leg	θ_{along}	θ_{cross}	θ_{leg}	θ_{rot}	$\cos(\theta_{rot})$
13 (N)	74.5	344.5	340.4	4.1	1.00
14	83.7	353.7	344.1	9.6	0.99
17	109.5	19.5	343.7	35.8	0.81
19	143.3	53.4	42.1	11.2	0.98
20 (NE)	157.6	67.6	52.8	14.8	0.97
21	179.2	89.3	51.2	38.1	0.79
22	200.5	110.5	101.1	9.4	0.99
23	200.5	110.5	127.2	-16.7	0.96
24	202.1	112.1	119.3	-7.1	0.99
25	206.4	116.4	131.9	-15.5	0.96
26 (E)	209.5	119.5	132.9	-13.4	0.97
27	215.7	125.7	137.7	-12.1	0.98
28	216.0	126.0	121.9	4.1	1.00
29 (SE)	214.8	124.8	119.4	5.4	1.00
32	232.1	142.1	169.6	-27.5	0.89
33	240.7	150.7	170.2	-19.4	0.94
35 (S)	284.2	194.2	179.9	14.3	0.97
36	296.8	206.8	179.4	27.4	0.89
37	296.5	206.5	179.8	26.7	0.89
38	305.8	215.8	179.4	36.3	0.81
39	309.2	219.2	180.1	39.1	0.78
40	311.5	221.5	189.8	31.7	0.85
41	26.0	296.0	325.4	-29.4	0.87
43	53.1	323.1	1.7	38.6	0.78
44	71.2	341.2	345.1	-3.9	1.00

LIST OF FIGURES

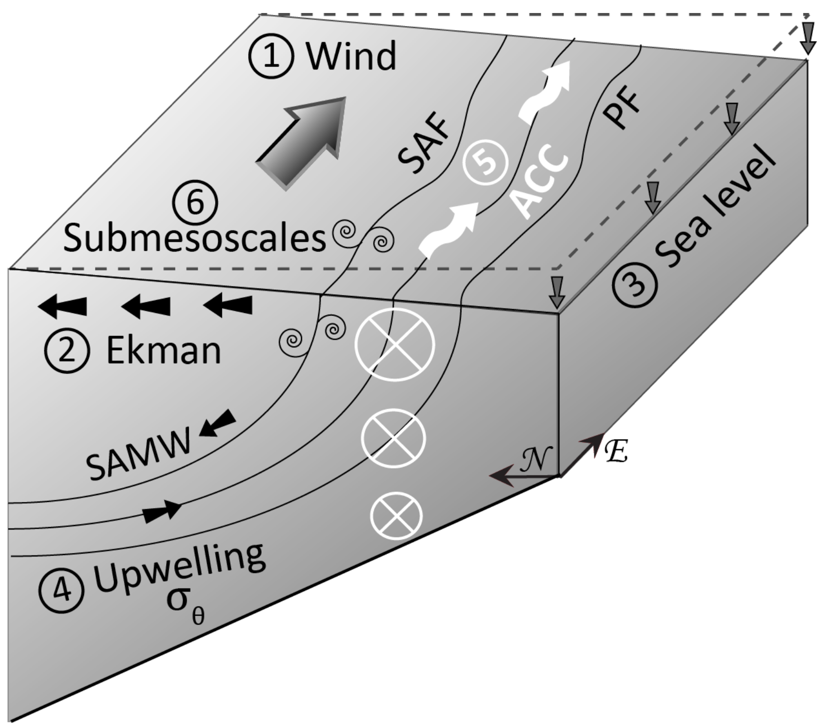

594 FIG. 1. Schematic of wind-driven upwelling in the Southern Ocean. The Antarctic Circumpolar Current (ACC), Subantartic and Polar fronts (SAF, PF) and Subantarctic Mode water (SAMW) locations are labeled.

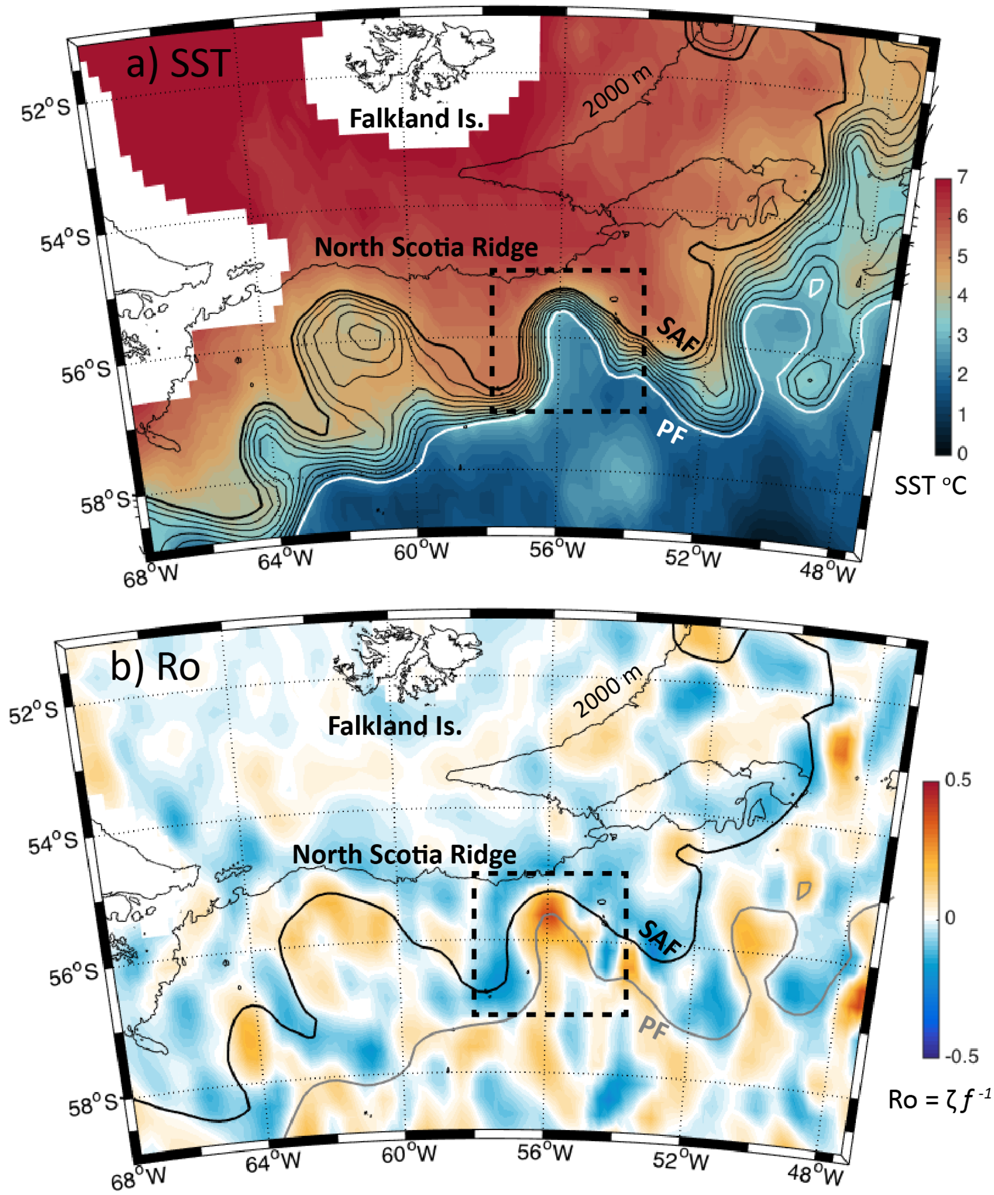

FIG. 2. a) A northward meander (dashed box) of the ACC in the Scotia Sea observed remotely on 20 April 2015 is characterized by sharp horizontal gradients of SST (°C; color) and SSH (m; contours). b) Same for vorticity Rossby number (color) calculated from altimetry-derived geostrophic surface currents for 20 April 2015. SSH contours corresponding to the Subantarctic (SAF; -0.25 m) and Polar (PF; -0.70 m) fronts define the northern and southern edges of the meander, respectively. The 2000-m isobath from GEBCO outlines the North Scotia Ridge, the northern boundary of the Scotia sea.

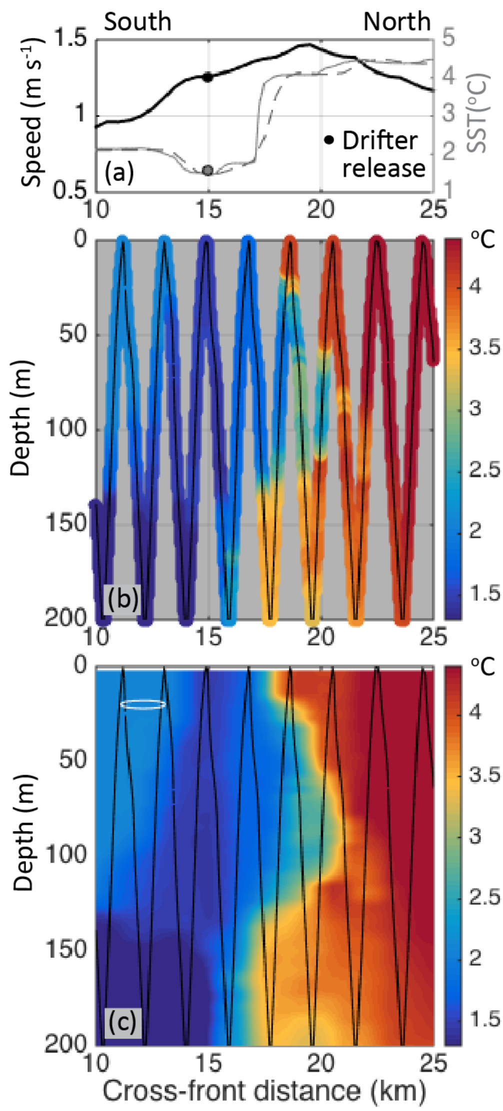

FIG. 3. a) Measured jet speed (m s^{-1}) at 50-m depth and underway SST (°C) at 4-m depth during the first Seasoar leg in survey. Gridded Seasoar temperature at 5-m depth is dashed. Drifters were released in the cold filament (1.56 °C) with jet speed $\sim$ 1.25 m s^{-1}, approximately 15 km from the start of the Seasoar leg. b) Temperature data binned into 0.5-m intervals for the first Seasoar leg. c) Same as (b) for gridded temperature data with the interpolation window, 2 km by 4 m, shown as an ellipse (white). The location of Seasoar measurements in (b) and (c) are black.

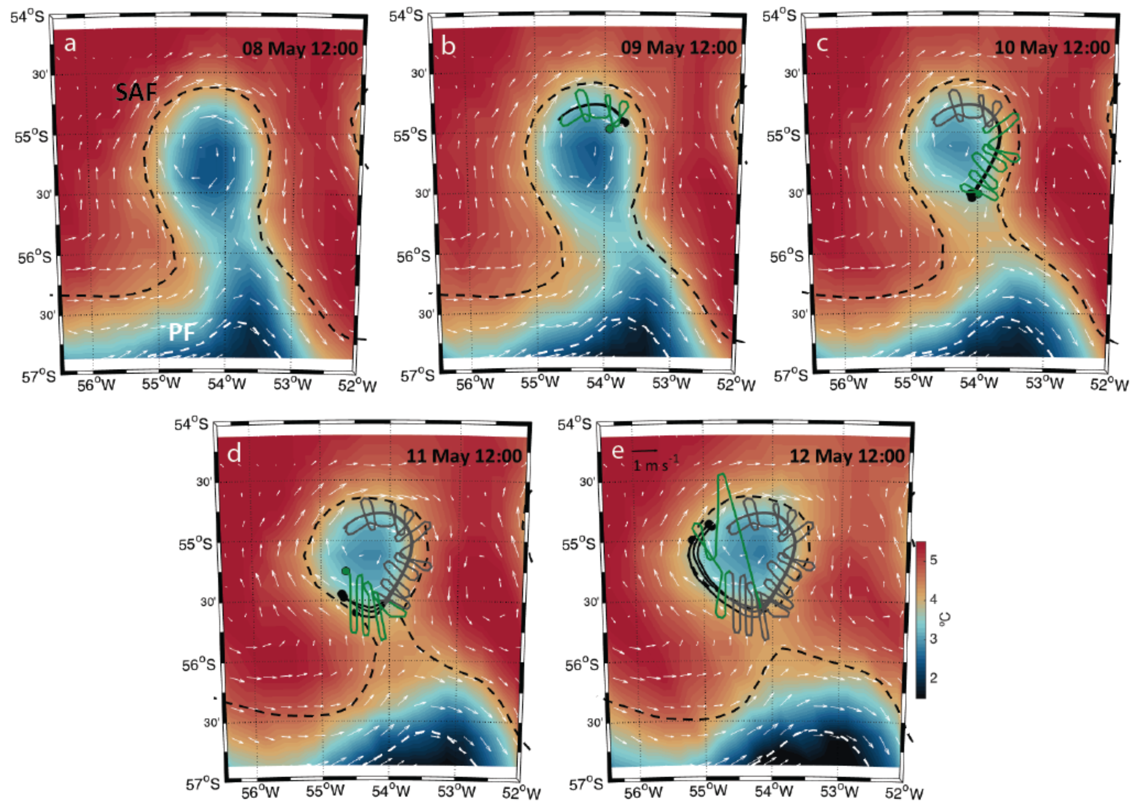

FIG. 4. Daily snapshots of microwave SST (REMSS) and altimetric geostrophic surface current vectors (AVISO) for 8 to 12 May 2015 capturing the formation of a mesoscale eddy from a northward meander along the ACC in the Scotia Sea (Figure 2). A drifter triplet shown in black was released on 08 May 20:00 GMT in the northwestern sector of the meander and followed whilst towing Seasoar with the RRS JCR (green). Positions of the SAF and PF, defined by the -0.25-m and -0.70-m SSH contours, are shown in black and white dashed lines, respectively.

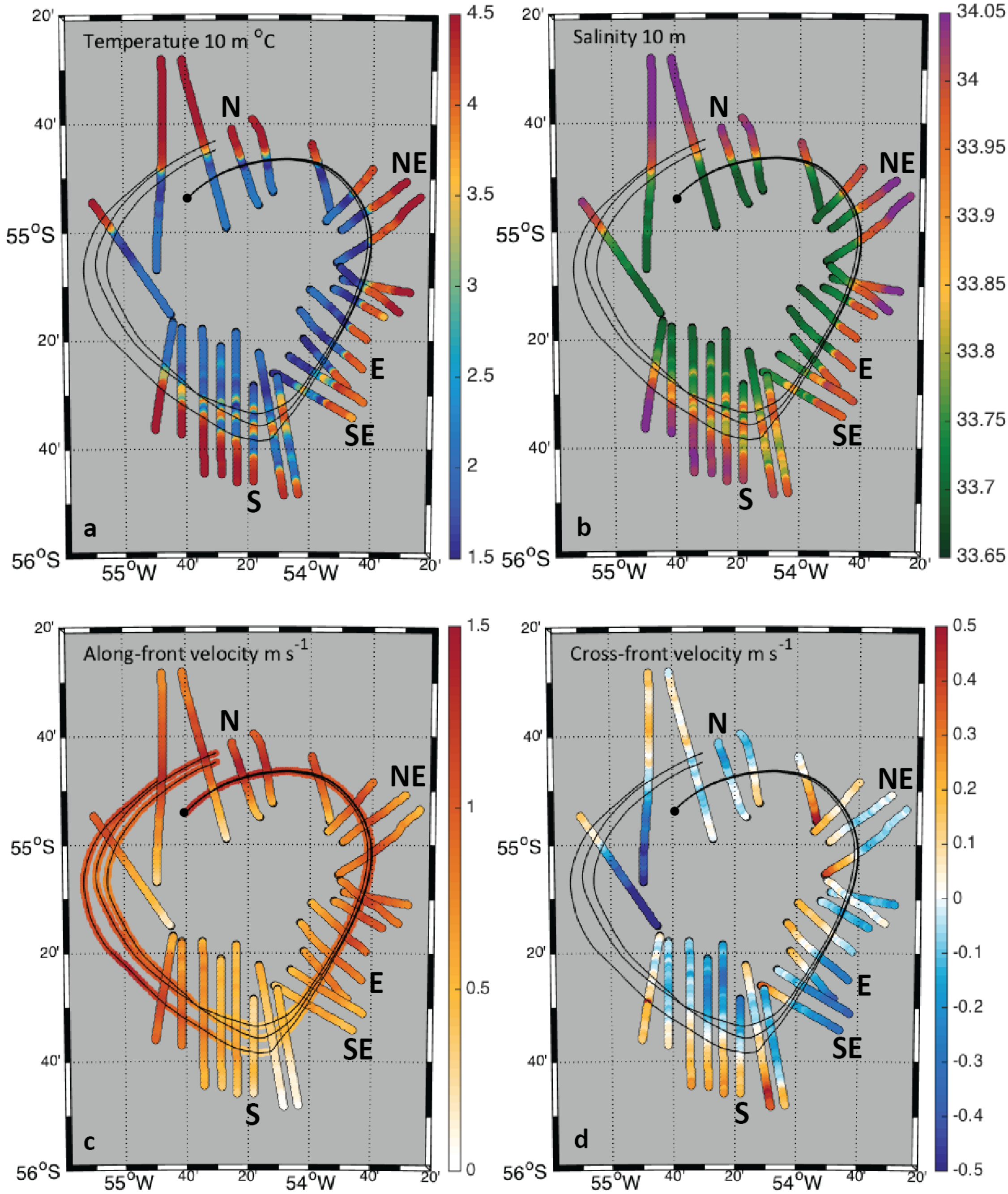

FIG. 5. Maps of 10-m depth (a) temperature and (b) salinity and 50-m depth (c) along-front and (d) cross-front velocity measurements from the drifter-following Seasoar survey introduced in Figure 4. A circle marks the starting position of the cyclonic survey. Drifter triplet tracks are shown in black except in (c) where drifter speed is also in color. Positive along-front velocities indicate a cyclonic (clockwise) direction where as positive cross-front velocities indicate flow out of the eddy. Labeled Seasoar legs, indicating the approximate location in the survey, are presented in Figure 7.

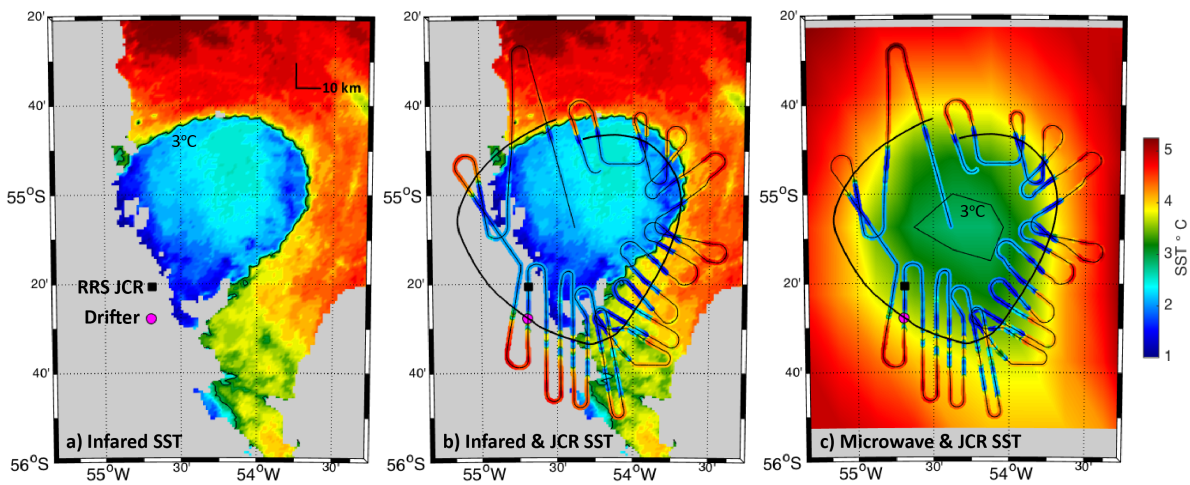

FIG. 6. (a) Level 2 infared SST measured at 11 May 2015 12:42 GMT by an AVHRR sensor with 1-km horizontal resolution on the Metop-a satellite as the drifters (•) and the RRS JCR (■) were completing the southwest sector of the Seasoar survey. (b) JCR underway temperature data measured during the survey at 4-m depth and 40-m horizontal resolution overlaid on (a). A drifter track (black) is included. (c) Same as (b) overlaid on microwave SST (OISST; www.remss.com). The 3°C isotherm (black) outlines the eddy edge in (a) and the eddy center in (c).

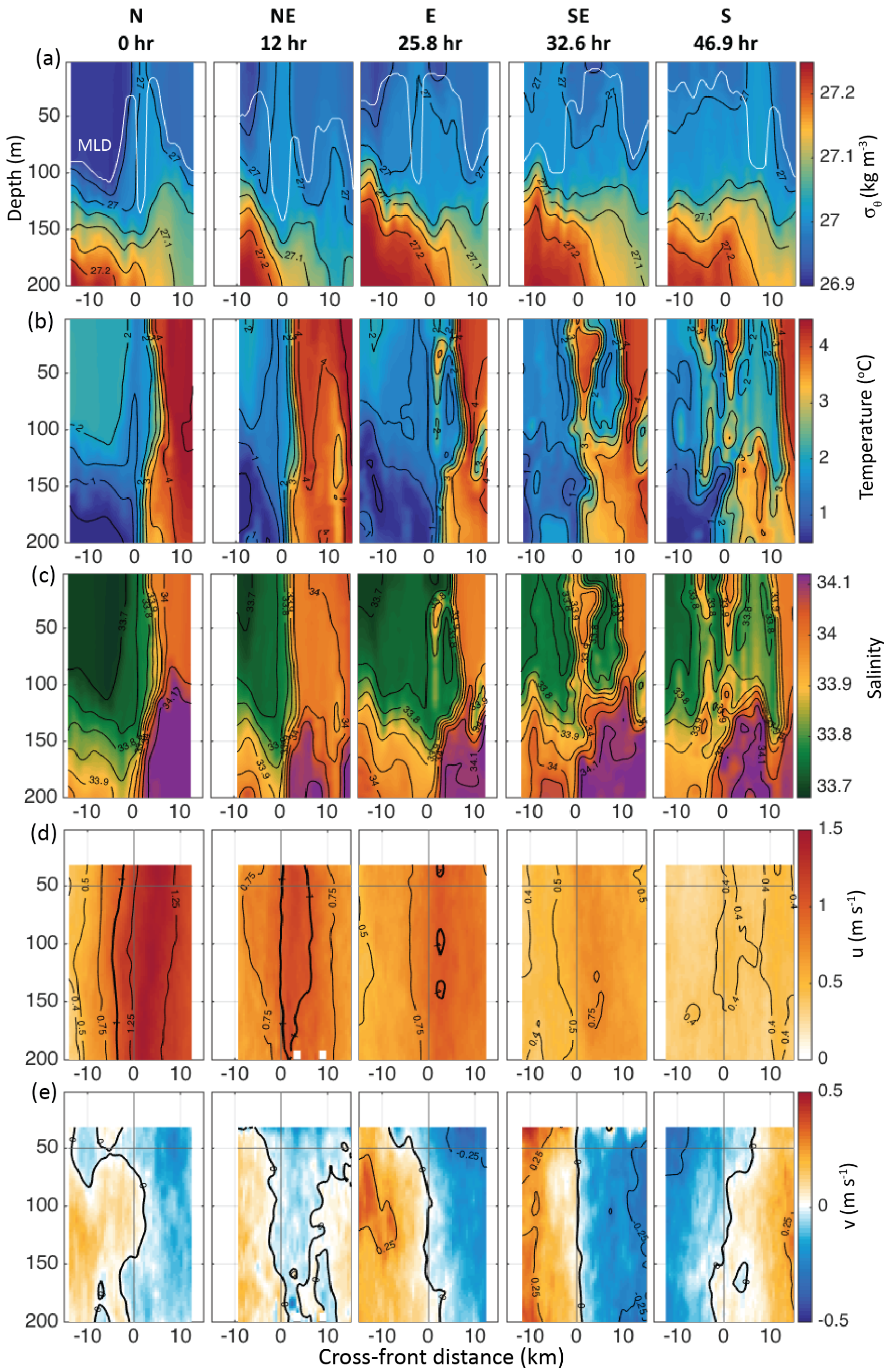

626 FIG. 7. Vertical cross-front sections of (a) potential density anomaly (kg m^{-3}), (b) temperature (°C), (c)
627 salinity, (d) along-front velocity and (e) cross-front velocity for Seasoar legs N to S. The start time since the
628 start of leg N is reported above (a) in hours. Sections are oriented such that cross-front distance increases away
629 from the meander and eddy center. Mixed layer depth (MLD) defined as a 0.01 kg m^{-3} density difference from
630 the surface is white in (a). The drifter location during each leg is at cross-front distance = 0 and depth = 50 m,
631 shown at the intersection of gray lines in (c) and (d).

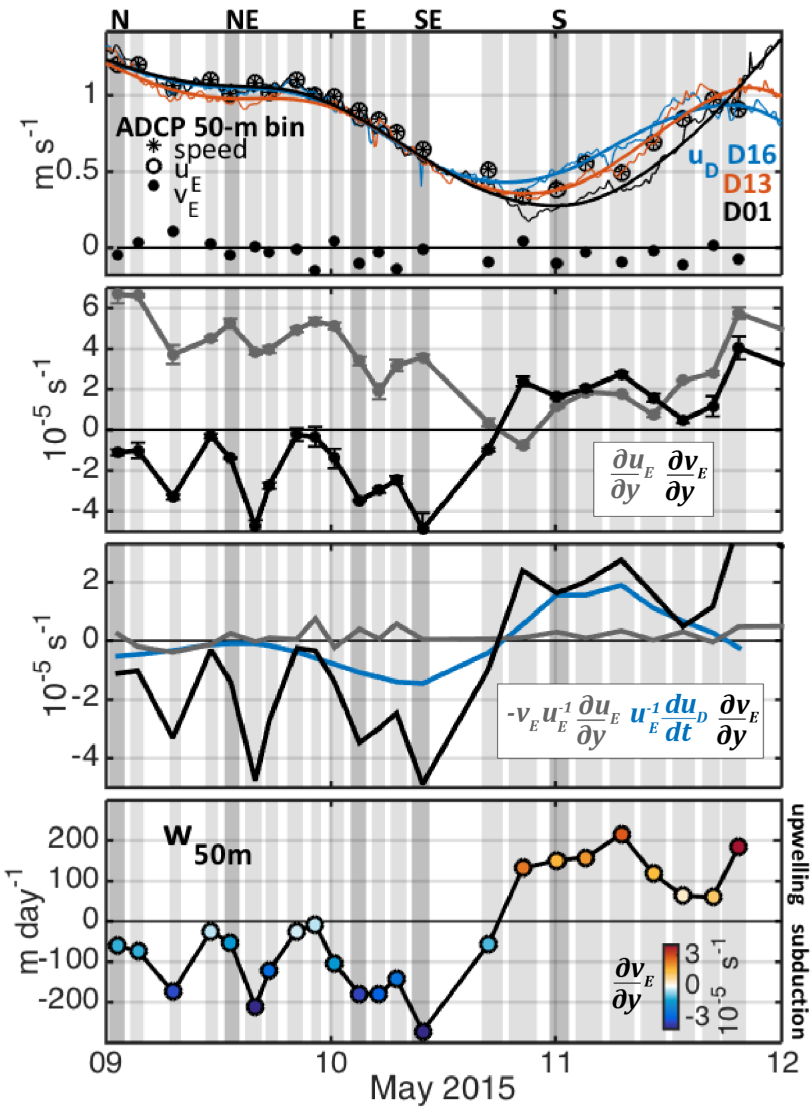

FIG. 8. (a) Time series of along-front drifter velocity, u^D (m s^{-1}), for the three drifters released and followed during the Seasoar survey from 9 to 12 May 2015. Along-front, x, and cross-front, y, water velocity components, u_E and v_E, measured within 1 km of the frontal center are shown for the drifter drogue depth of 50 m. Water speed (*) is also included to show the good agreement with u_E. (b) Cross-front gradients of u_E (gray) and v_E (black) at 50-m depth and averaged +/- 1 km across the front. Standard deviations of $\frac{\partial \bar{u}_E}{\partial y}$ and $\frac{\partial \bar{v}_E}{\partial y}$ are shown across the 10-m drogue depth, 45-55 m. Negative $\frac{\partial \bar{v}_E}{\partial y}$ (black) indicates confluent flow. (c) Estimation of terms in Equation 12 after making steady-state assumption. (d) Vertical velocity at the drogue depth of 50 m, $w_{50\mathrm{m}}$ (m day^{-1}), with $\frac{\partial \bar{v}_E}{\partial y}$, or lateral divergence (s^{-1}), from panel (b) shown in color. Vertical velocities and $\frac{\partial \bar{v}_E}{\partial y} < 0$ indicate subduction and confuence, respectively. The duration of individual Seasoar legs is shaded in each panel.

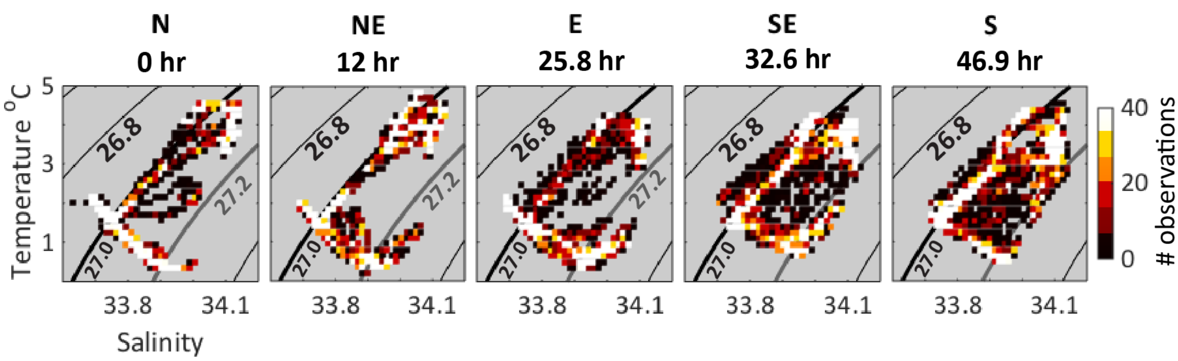

641 FIG. 9. T-S diagram histograms for Seasoar legs N to S. Color indicates number of measurements in 0.15°C
642 and 0.015 salinity bins. The cold, fresh observations inside the meander and eddy occupy the bottom left 'hot
643 spot' of measurements in T-S space in Leg N. An exchange along isopycnals $\sigma_{\theta 27}$ (bold) and $\sigma_{\theta 27.2}$ (gray)
644 occurs over this series.

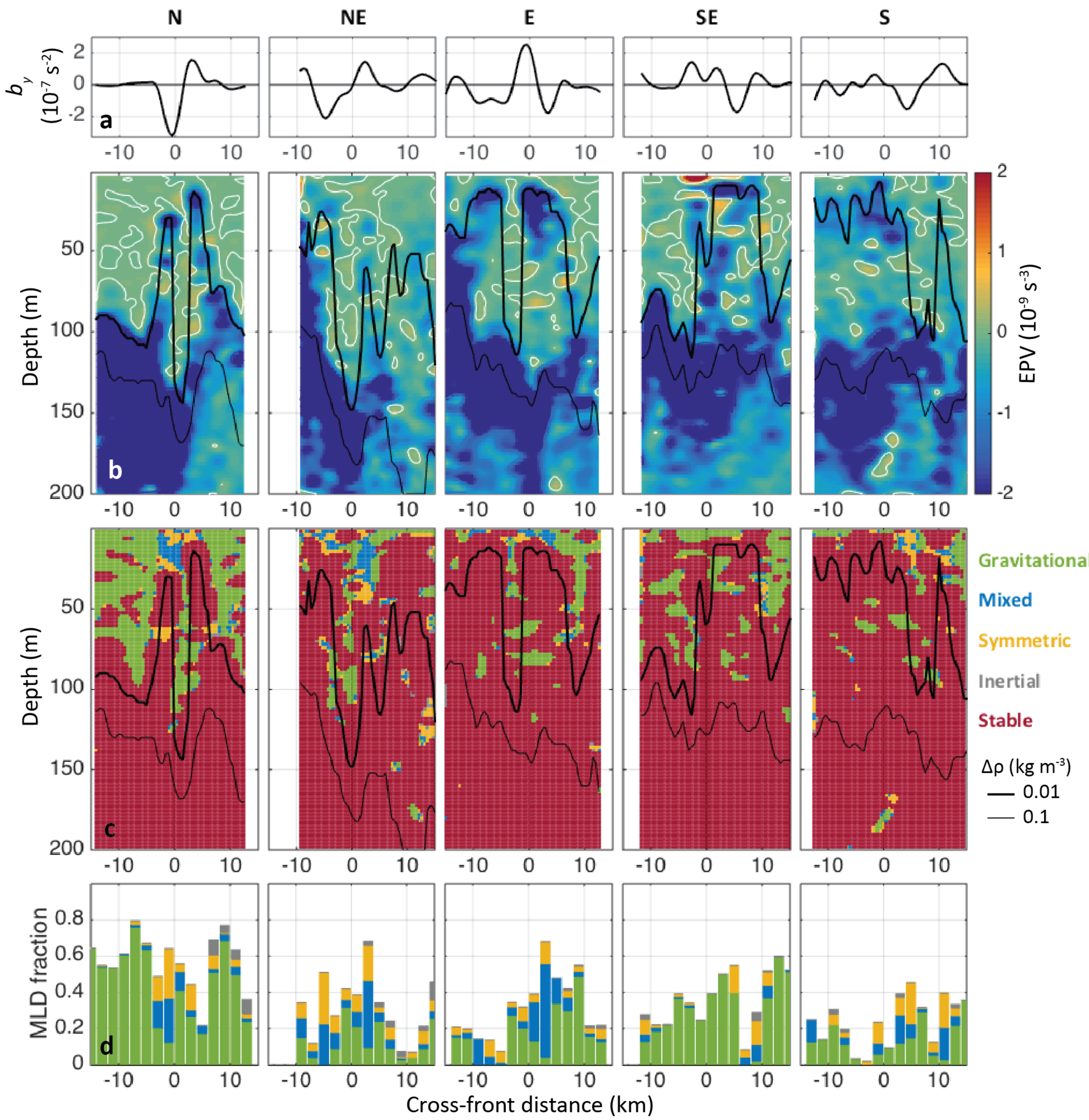

645 FIG. 10. (a) Cross-front buoyancy gradient, b_y, (s^{-2}) calculated at 10-m water depth for Seasoar legs N to S. Legs are oriented with the inside of the meander and eddy on the left-hand side of each panel. (b) A 2-dimensional estimate of Ertel potential vorticity (s^{-3}) is shown with the zero contour in white and the MLD, defined as a 0.01 (0.1) kg m^{-3} density difference from the surface, as a thick (thin) black line. (c) Submesoscale instability analysis results based on the Ri_B criteria. (d) Instances of instabilities identified in (c) shown as a fraction of the 0.01 kg m^{-3} density difference MLD.

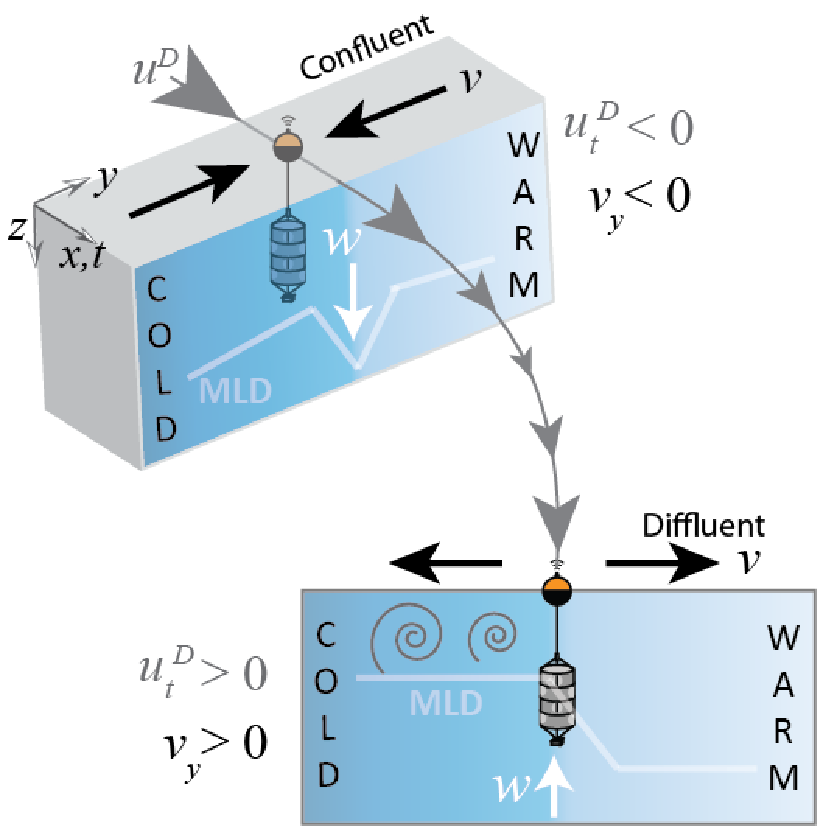

651 FIG. 11. Cartoon summarizing frontal circulation during eddy formation. The two cross-frontal sections
652 represent the northern and southern sectors of the survey, legs N and S.